INTERNATIONAL JOURNAL OF
NUMERICAL ANALYSIS AND MODELING
Volume 13, Number 4, Pages 587–609

ASSESSMENT OF TWO APPROXIMATION METHODS FOR THE INVERSE PROBLEM OF ELECTROENCEPHALOGRAPHY

A. ALONSO-RODRÍGUEZ, J. CAMAÑO, R. RODRÍGUEZ, AND A. VALLI

Abstract. The goal of this paper is to compare two computational models for the inverse problem of electroencephalography: the localization of brain activity from measurements of the electric potential on the surface of the head. The source current is modeled as a dipole whose localization and polarization has to be determined. Two methods are considered for solving the corresponding forward problems: the so called *subtraction approach* and *direct approach*. The former is based on subtracting a fundamental solution, which has the same singular character of the actual solution, and solving computationally the resulting non-singular problem. Instead, the latter consists in solving directly the problem with singular data by means of an adaptive process based on an a posteriori error estimator, which allows creating meshes appropriately refined around the singularity. A set of experimental tests for both, the forward and the inverse problems, are reported. The main conclusion of these tests is that the direct approach combined with adaptivity is preferable when the localization of the dipole is close to an interface between brain tissues with different conductivities.

Key words. Electroencephalography, dipole source, electrostatics, inverse problem.

1. Introduction

Electroencephalography (EEG) is a diagnostic procedure which measures the electrical activity of the brain, by means of electrodes placed on the scalp. This non-invasive technique can be used for localizing current sources in the human brain [13].

Electromagnetic cerebral activity is due to the motion of ions in the active regions of the brain. This movement generates the so called *impressed current* (or primary current) that in turn creates ohmic currents in the surrounding environment called *return currents*. We are interested in determining the impressed current.

The reconstruction of the position and of some physical characteristics of the current density that gives rise to the EEG measurements is called the inverse problem. For an accurate reconstruction of the primary current it is important to be able to model realistically tissue conductivity inhomogeneities.

Since the frequency spectrum for electrophysiological signals in EEG is below 1,000 Hz, often between 0.1 and 100 Hz, most theoretical works on biomedical applications such as [8, 10, 22, 14] use the *static approximation of the Maxwell equations* in which the time variation of both electric and magnetic fields are disregarded. The static model is not the only possible simplification of the Maxwell equations. Other models that can be taken into account are the *electro-quasistatic model*, in which the time variation of the magnetic induction is not considered and the *magneto-quasistatic model* or *eddy current equations*, which are derived from the Maxwell equations by neglecting the time derivative of the electric field. It is also possible to study the problem using the *full system of Maxwell equations*. Some references on these approaches are [2, 1, 4, 11].

Received by the editors June 5, 2014, and, in revised form, January 5, 2016.
2000 *Mathematics Subject Classification.* 65J22, 65L50.

We focus on the static model which leads to the electrostatics problem. We consider two strategies to approximate the potential for the electrostatics problem by using FEM. One of them is the "subtraction approach" which has been studied in [21, 22, 12, 9, 6, 19, 16], for example. In this formulation it is necessary to assume that the dipole is located in a region with a homogeneous conductivity. Then, it is possible to consider a more regular unknown, namely, the difference between the total potential and the fundamental solution with constant conductivity, which allows us to overcome the difficulties arising from the singularity of the source. Let us remark that this is a frequently used finite element approach for the numerical modeling in EEG.

The other method is the "direct approach", in which the unknown is the total potential and the dipole source is incorporated directly in the weak formulation which is solved by a finite element method. These two approaches have been compared in [5] in terms of computational complexity and accuracy. More recently, the direct approach was further analyzed in [3], where an a posteriori error estimate and an adaptive scheme which allows improving its efficiency were also introduced.

In this paper we report some numerical computations in order to compare the two methods: the well-known subtraction approach and the direct approach with adaptivity. The former is usually less expensive in terms of computational cost, because its solution does not present singularities and, consequently, coarse uniform meshes can be used for its finite element solution. However, we show that this is not always the case. In particular, we use them for the approximation of the inverse problem when the conductivity has a jump across the interface between different tissues (we recall that this is the case in the real physiological framework). We study in particular the case of a dipolar source located close to the interface between two regions with different conductivities (which again is physiologically realistic). The reported tests show that, in such a case, the subtraction approach can suffer from severe instabilities, while the direct approach is fairly stable. The instability of the subtraction approach is evident even for a two-dimensional problem with a simple geometry, and it seems that can be cured only on very fine meshes. Therefore, the instability clearly becomes more important when the problem is set in three dimensions on a more complex geometrical situation, since in that case very fine meshes are significantly more difficult to handle.

The paper is organized as follows: in Section 2 we introduce the methods and the assumptions to obtain well-posed problems, we establish some a priori error estimates and, finally, we introduce the a posteriori error estimator for the direct approach. In Section 3, we analyze the performances of the subtraction method and the direct approach with adaptivity for the corresponding forward problem. In Section 4 we explain in detail how we solve the inverse problem. In Section 5 we focus on how we generate reliable measurements for the simulations. In Section 6 we report numerical results for the inverse problem and, finally, in Section 7 we draw some conclusions.

2. Two approximation methods

We start introducing the equations.

2.1. Continuous problem. In almost all the studies concerning the neural generation of electromagnetic fields the static approximation of Maxwell equations is

considered:

$$(1)\qquad \begin{cases} \operatorname{div} \boldsymbol{D} = \rho\,, \\ \mathbf{curl}\, \boldsymbol{E} = \mathbf{0}\,, \\ \mathbf{curl}\, \boldsymbol{H} = \boldsymbol{J}\,, \\ \operatorname{div} \boldsymbol{B} = 0\,, \end{cases}$$

where $\boldsymbol{E}$ and $\boldsymbol{D}$ are the electric field and electric displacement, respectively, ρ the electric charge density and $\boldsymbol{J}$ the electric current density. By $\boldsymbol{H}$ and $\boldsymbol{B}$ we denote the magnetic field and the magnetic induction, respectively. A detailed justification of the choice of the static model in this context can be found for instance in Plonsey & Heppner [17].

For biological tissues, the linear constitutive equations $\boldsymbol{D} = \boldsymbol{\varepsilon}\boldsymbol{E}$ and $\boldsymbol{B} = \boldsymbol{\mu}\boldsymbol{H}$ can be assumed (see, for instance, [4, 1]), where $\boldsymbol{\varepsilon}$ and $\boldsymbol{\mu}$ correspond to the electric permittivity and the magnetic permeability, respectively.

From the second equation of (1), we conclude that there exists a scalar potential u such that $\boldsymbol{E} = -\nabla u$. From Ohm law, the total current density $\boldsymbol{J}$ is the sum of the impressed current plus the return currents

$$\boldsymbol{J} = \boldsymbol{J}_p + \boldsymbol{\sigma}\boldsymbol{E} = \boldsymbol{J}_p - \boldsymbol{\sigma}\nabla u\,,$$

where $\boldsymbol{\sigma}$ is the conductivity, which is a uniformly positive definite matrix valued function with L^∞ entries.

From the third equation in (1) it follows that

$$0 = \operatorname{div} \boldsymbol{J} = \operatorname{div}(\boldsymbol{J}_p - \boldsymbol{\sigma}\nabla u)\,.$$

Hence u is solution of the equation

$$\operatorname{div}(\boldsymbol{\sigma}\nabla u) = \operatorname{div} \boldsymbol{J}_p\,.$$

We consider a domain Ω, open, connected and bounded, with Lipschitz continuous boundary $\partial\Omega$ included in $\mathbb{R}^d$, where $d = 2$ or $d = 3$ (Ω represents the human head for $d = 3$ or a two-dimensional section for $d = 2$). We define $\boldsymbol{n}$ to be the outer unit normal vector on $\partial\Omega$. We assume that $\boldsymbol{J}_p$ is supported in Ω. Since $\boldsymbol{J}|_\Omega \cdot \boldsymbol{n} = \boldsymbol{J}|_{\mathbb{R}^d \setminus \overline{\Omega}} \cdot \boldsymbol{n} = 0$ on the interface $\partial\Omega$ and $\boldsymbol{J}_p \cdot \boldsymbol{n} = 0$ on $\partial\Omega$, it follows that $(\boldsymbol{\sigma}\nabla u) \cdot \boldsymbol{n} = 0$ on $\partial\Omega$. Then, we obtain this problem:

$$\begin{cases} \operatorname{div}(\boldsymbol{\sigma}\,\nabla u) = \operatorname{div} \boldsymbol{J}_p & \text{in } \Omega\,, \\ (\boldsymbol{\sigma}\nabla u) \cdot \boldsymbol{n} = 0 & \text{on } \partial\Omega\,. \end{cases}$$

Let us assume that there is a small activated region centered at a point $\boldsymbol{x}_0$ and that the observation points are far from it. In this case the primary current $\boldsymbol{J}_p$ is typically modeled as a dipole $\boldsymbol{p}\delta_{\boldsymbol{x}_0}$, where $\delta_{\boldsymbol{x}_0}$ is the Dirac delta distribution centered at $\boldsymbol{x}_0$ (see [22]). So, in the following, we consider the electrostatic problem above with a dipole source term:

$$(2)\qquad \begin{cases} \operatorname{div}(\boldsymbol{\sigma}\,\nabla u) = \operatorname{div}(\boldsymbol{p}\,\delta_{\boldsymbol{x}_0}) & \text{in } \Omega\,, \\ (\boldsymbol{\sigma}\nabla u) \cdot \boldsymbol{n} = 0 & \text{on } \partial\Omega\,, \end{cases}$$

where $\boldsymbol{x}_0$ is an inner point of Ω, and $\boldsymbol{p} \neq \mathbf{0}$ is the polarization vector. In [18] the existence and uniqueness of solution $u \in L^p(\Omega)$, $1 < p < 3/2$, of this problem (for

$d = 3$) has been studied under the assumption of some additional regularity of $\boldsymbol{\sigma}$ in a vicinity of $\boldsymbol{x}_0$. We recall that for $p \geq 1$,

$$L^p(\Omega) := \left\{ v : \Omega \to \mathbb{R} \, : \, \int_\Omega |v|^p < \infty \right\}$$

is a vector space endowed with the norm

$$\|v\|_{0,p,\Omega} := \left(\int_\Omega |v|^p \right)^{1/p}.$$

We will give more details below.

The singularity of the dipole source can be treated by using the so-called *subtraction approach*. In what follows we explain this technique. For using it, we need to assume that there exists a nonempty open subdomain $\Omega_0 \subset \Omega$ around the source position $\boldsymbol{x}_0$ with constant conductivity $\boldsymbol{\sigma}_0$ (in general, a matrix). The conductivity $\boldsymbol{\sigma}$ is then split into two parts,

$$\boldsymbol{\sigma} = \boldsymbol{\sigma}_0 + \boldsymbol{\sigma}_s \,, \tag{3}$$

so that $\boldsymbol{\sigma}_0$ is constant over the whole domain Ω and $\boldsymbol{\sigma}_s$ vanishes in the subdomain Ω_0. The total potential u is also split into two parts:

$$u = u_0 + u_s, \tag{4}$$

where u_0 satisfies

$$\operatorname{div}(\boldsymbol{\sigma}_0 \nabla u_0) = \operatorname{div}(\boldsymbol{p}\, \delta_{\boldsymbol{x}_0}). \tag{5}$$

An analytic formula for u_0 in the case of a homogeneous conductivity $\boldsymbol{\sigma}_0$ is known (see [15]) :

$$u_0(\boldsymbol{x}) = \begin{cases} \dfrac{\boldsymbol{p}^t \boldsymbol{\sigma}_0^{-1}(\boldsymbol{x} - \boldsymbol{x}_0)}{2\pi\sqrt{\det \boldsymbol{\sigma}_0}(\boldsymbol{x} - \boldsymbol{x}_0)^t \boldsymbol{\sigma}_0^{-1}(\boldsymbol{x} - \boldsymbol{x}_0)}, & \text{if } d = 2\,, \\ \dfrac{\boldsymbol{p}^t \boldsymbol{\sigma}_0^{-1}(\boldsymbol{x} - \boldsymbol{x}_0)}{4\pi\sqrt{\det \boldsymbol{\sigma}_0}\left((\boldsymbol{x} - \boldsymbol{x}_0)^t \boldsymbol{\sigma}_0^{-1}(\boldsymbol{x} - \boldsymbol{x}_0)\right)^{3/2}}, & \text{if } d = 3\,. \end{cases}$$

The above expression simplifies as follows when the medium is isotropic (i.e., $\boldsymbol{\sigma}_0 = \sigma_0 \boldsymbol{I}$ with σ_0 a constant) :

$$u_0(\boldsymbol{x}) = \begin{cases} \dfrac{\boldsymbol{p}^t(\boldsymbol{x} - \boldsymbol{x}_0)}{2\pi\sigma_0|\boldsymbol{x} - \boldsymbol{x}_0|^2}, & \text{if } d = 2\,, \\ \dfrac{\boldsymbol{p}^t(\boldsymbol{x} - \boldsymbol{x}_0)}{4\pi\sigma_0|\boldsymbol{x} - \boldsymbol{x}_0|^3}, & \text{if } d = 3\,. \end{cases}$$

Replacing (3) and (4) in (2) and using that u_0 satisfies (5), we obtain

$$\operatorname{div}[(\boldsymbol{\sigma}_0 + \boldsymbol{\sigma}_s)\nabla(u_0 + u_s)] = \operatorname{div}(\boldsymbol{p}\, \delta_{\boldsymbol{x}_0}) = \operatorname{div}(\boldsymbol{\sigma}_0 \nabla u_0)\,,$$

and hence

$$\operatorname{div}(\boldsymbol{\sigma}\nabla u_s) = \operatorname{div}[(\boldsymbol{\sigma}_0 + \boldsymbol{\sigma}_s)\nabla u_s] = -\operatorname{div}(\boldsymbol{\sigma}_s \nabla u_0)\,.$$

On the other hand, since

$$0 = (\boldsymbol{\sigma}\nabla u) \cdot \boldsymbol{n} = (\boldsymbol{\sigma}\nabla(u_0 + u_s)) \cdot \boldsymbol{n} \quad \text{on } \partial\Omega\,,$$

we derive the Neumann boundary condition

$$(\boldsymbol{\sigma}\nabla u_s) \cdot \boldsymbol{n} = -(\boldsymbol{\sigma}\nabla u_0) \cdot \boldsymbol{n} \quad \text{on } \partial\Omega\,.$$

In conclusion, u_s solves the boundary value problem

$$
(6)\qquad \begin{cases} \operatorname{div}(\boldsymbol{\sigma}\,\nabla u_s) = -\operatorname{div}(\boldsymbol{\sigma}_s \nabla u_0) & \text{in } \Omega\,, \\ (\boldsymbol{\sigma}\nabla u_s)\cdot \boldsymbol{n} = -(\boldsymbol{\sigma}\nabla u_0)\cdot \boldsymbol{n} & \text{on } \partial\Omega\,, \\ \displaystyle\int_\Omega u_s = 0\,. \end{cases}
$$

The last condition of (6) filters out additive constants and therefore is suitable for ensuring uniqueness of the solution u_s. In practice, any other condition with the same property could be alternatively used.

The goal of this formulation is to obtain a problem with a more regular source, in order to eliminate the singularity of the solution at $\boldsymbol{x}_0$. Noting that the potential u_0 has a singularity at $\boldsymbol{x} = \boldsymbol{x}_0$ but is smooth for $\boldsymbol{x} \neq \boldsymbol{x}_0$, we see that the Neumann datum in (6) is smooth and, moreover, since $\boldsymbol{\sigma}_s$ vanishes in Ω_0, we have that $\boldsymbol{\sigma}_s \nabla u_0 \in [L^\infty(\Omega)]^d$. Thus we are able to write the following variational formulation of problem (6):

Find $u_s \in H^1(\Omega)$:

$$
\begin{cases} \displaystyle\int_\Omega \boldsymbol{\sigma}\nabla u_s \cdot \nabla v = -\int_\Omega \boldsymbol{\sigma}_s \nabla u_0 \cdot \nabla v - \int_{\partial\Omega} \boldsymbol{\sigma}_0 \nabla u_0 \cdot \boldsymbol{n}\, v \quad \forall\, v \in H^1(\Omega)\,, \\ \displaystyle\int_\Omega u_s = 0\,. \end{cases}
$$

An alternative approach which allows relaxing the assumption that $\boldsymbol{\sigma}$ has to be constant in a neighborhood of $\boldsymbol{x}_0$ is the *direct approach* studied in [18]. It is based on a direct ultra weak formulation of problem (2), valid for sufficiently smooth test functions φ:

$$
\int_\Omega u\, \operatorname{div}(\boldsymbol{\sigma}\nabla\varphi) = -\boldsymbol{p}\cdot\nabla\varphi(\boldsymbol{x}_0).
$$

Under the assumption that the conductivity $\boldsymbol{\sigma}$ is sufficiently smooth in a neighborhood of $\boldsymbol{x}_0$, it was proved in [3] that the following problem has a unique solution: Find $u \in L^p(\Omega)$ such that

$$
(7)\qquad \begin{cases} \displaystyle\int_\Omega u\, \operatorname{div}(\boldsymbol{\sigma}\,\nabla\varphi) = -\boldsymbol{p}\cdot\nabla\varphi(\boldsymbol{x}_0) & \forall\,\varphi \in X\,, \\ \displaystyle\int_\Omega u = 0\,, \end{cases}
$$

where

$$
X := \{\varphi \in H^1(\Omega) :\ \varphi \in \mathcal{C}^1(B_{r*}(\boldsymbol{x}_0)),\ \operatorname{div}(\boldsymbol{\sigma}\nabla\varphi) \in L^q(\Omega),\ \text{and } (\boldsymbol{\sigma}\nabla\varphi)\cdot\boldsymbol{n} = 0 \text{ on } \partial\Omega\},
$$

being $r*$ a fixed number such that $0 < r* < r_0$. Moreover, here and thereafter $\frac{1}{p} + \frac{1}{q} = 1$. The proof in [18] is for $d = 3$, but it also holds true for $d = 2$, as shown in [3].

We summarize these results in the following theorem:

Theorem 2.1. *There exists a unique solution to* (7)*, which belongs to* $L^p(\Omega)$ *for* $1 < p < 3/2$ *in 3D (or* $1 < p < 2$ *in 2D).*

2.2. Discrete problem. In the remainder of this paper, we will focus on the 2D problem, for simplicity. However, the analysis extends readily to 3D problems.

Also for simplicity we assume that Ω is a polygon. We consider a regular family of triangular meshes $\mathcal{T}_h$ of Ω (see, for instance, [7]). As usual, h denotes the mesh

size: $h := \max_{T\in\mathcal{T}_h} h_T$, h_T being the diameter of T. We consider the standard space of Lagrange finite elements of degree one:

$$V_h := \{v_h \in \mathcal{C}(\Omega) \,:\, v_h|_T \in \mathcal{P}_1 \;\forall\, T \in \mathcal{T}_h\}\,.$$

The finite element approximation of the subtraction approach in [22] reads: find $u_{s,h} \in V_h$ such that

$$\text{(8)}\quad \begin{cases} \displaystyle\int_\Omega \boldsymbol{\sigma}\nabla u_{s,h}\cdot\nabla v_h = -\int_\Omega \boldsymbol{\sigma}_s\nabla u_0\cdot\nabla v_h - \int_{\partial\Omega}\boldsymbol{\sigma}_0\nabla u_0\cdot\boldsymbol{n}\, v_h \quad \forall\, v_h \in V_h\,, \\ \displaystyle\int_\Omega u_{s,h} = 0\,. \end{cases}$$

To prove the convergence of $u_{s,h}$ to u_s is straightforward (see [22]).

On the other hand, the finite element approximation of the direct approach reads: find $u_h \in V_h$ such that

$$\text{(9)}\quad \begin{cases} \displaystyle\int_\Omega \boldsymbol{\sigma}\nabla u_h\cdot\nabla v_h = \boldsymbol{p}\cdot\nabla(v_h|_{T_0})(\boldsymbol{x}_0) \qquad \forall\, v_h \in V_h\,, \\ \displaystyle\int_\Omega u_h = 0\,, \end{cases}$$

where T_0 is the triangle in $\mathcal{T}_h$ that contains $\boldsymbol{x}_0$. If there is more than one triangle containing $\boldsymbol{x}_0$, anyone of them can be chosen as T_0.

Remark 2.2. Since we are using piecewise linear elements, $\nabla(v_h|_{T_0})$ is a constant vector on the whole T_0. Therefore, the solution u_h of problem (9) is insensitive to the specific location of the point $\boldsymbol{x}_0 \in T_0$.

Under certain restrictive assumptions the following a priori error estimate has been proved in [3]:

Theorem 2.3. *Let $\mathcal{T}_h$ be a quasiuniform family of subdivisions of a convex Lipschitz polygon Ω and assume that $\sigma_{i,j} \in \mathcal{C}^1(\overline{\Omega})$, for each $i,j = 1,2$. Let u and u_h be the respective solutions to problems* (7) *and* (9)*. Then, there exists $h_0 > 0$ and $q_0 > 2$ such that*

$$\|u - u_h\|_{0,p,\Omega} \le Ch^{2/p-1}$$

for all $0 < h < h_0$ and for all p such that $\frac{q_0}{q_0-1} < p < 2$. Moreover, for $1 \le p \le \frac{q_0}{q_0-1}$ there holds

$$\|u - u_h\|_{0,p,\Omega} \le Ch^s$$

for all $0 < h < h_0$ and for all s with $0 < s < 1 - \frac{2}{q_0}$.

The value $q_0 > 2$ in this theorem is the maximal regularity exponent of the dual problem to (7), namely, the maximal value q_0 such that, given $\psi \in L^q(\Omega)$ with $q \in (2, q_0)$, the solution φ to

$$\begin{cases} \operatorname{div}(\boldsymbol{\sigma}\,\nabla\varphi) = \psi - \dfrac{1}{|\Omega|}\displaystyle\int_\Omega \psi & \text{in } \Omega\,, \\ (\boldsymbol{\sigma}\nabla\varphi)\cdot\boldsymbol{n} = 0 & \text{on } \partial\Omega\,, \\ \displaystyle\int_\Omega \varphi = 0\,, \end{cases}$$

belongs to $W^{2,q}(\Omega)$.

As stated above, the only aim of the last equation in problems (8), (9) is to have uniqueness of solution for these problems. However, in practice it is more reasonable to consider an alternative. Since typically the measurements in EEG are electric

potential differences with respect to one fixed electrode, it is more realistic (and simpler) to use

$$u(\boldsymbol{x}_{ref}) = 0$$

as the condition to determine a unique solution of these problems, where $\boldsymbol{x}_{ref}$ is the localization of the fixed electrode.

We can improve the results obtained with the direct approach by using meshes properly refined around $\boldsymbol{x}_0$. For the direct approach, the following residual-type a posteriori error estimator in $L^p(\Omega)$-norm has been proposed in [3] for the finite element approximation error $\|u - u_h\|_{0,p,T}$.

For all $T \in \mathcal{T}_h$ we define

$$\varepsilon_{T,p} := \left(h_T^{2p} \| \operatorname{div}(\boldsymbol{\sigma} \nabla u_h) \|_{0,p,T}^p + \frac{1}{2} \sum_{\ell \in \mathcal{E}(T) \cap \mathcal{E}_{h,i}} |\ell|^{p+1} \| [\![\boldsymbol{\sigma} \nabla u_h \cdot \boldsymbol{n}]\!] \|_{0,p,\ell}^p \right.$$
$$\left. + \sum_{\ell \in \mathcal{E}(T) \cap \mathcal{E}_{h,e}} |\ell|^{p+1} \| \boldsymbol{\sigma} \nabla u_h \cdot \boldsymbol{n} \|_{0,p,\ell}^p \right)^{1/p},$$

where $\mathcal{E}_{h,i}$ is the set of all the inner edges of the triangulation $\mathcal{T}_h$, $\mathcal{E}_{h,e}$ is the set of boundary edges, $\mathcal{E}(T)$ is the set of the edges of T and $[\![g]\!]$ denotes the jump of g across an edge. We define the local a posteriori error indicator $\eta_{T,p}$ for all $T \in \mathcal{T}_h$ as follows:

$$\eta_{T,p} := \begin{cases} \left(h_0^{2-p} + \varepsilon_{T,p}^p \right)^{1/p} & \text{if } T = T_0\,, \\ \varepsilon_{T,p} & \text{otherwise}\,, \end{cases} \tag{10}$$

where we denote by T_0 the triangle containing the point $\boldsymbol{x}_0$ used in (9) and by h_0 its diameter.

Next, we define the global error estimator from these indicators as follows:

$$\eta_p := \left(\sum_{T \in \mathcal{T}_h} \eta_{T,p}^p \right)^{1/p}.$$

Under suitable assumptions, among them $\boldsymbol{\sigma} \in [\mathcal{C}^1(\overline{\Omega})]^{2\times 2}$ and Ω a convex polygon, it has been proved in [3] that this estimator is reliable and efficient for any $p \in \left(\frac{q_0}{q_0 - 1}, 2 \right)$. Let us remark that the efficiency was actually proved for all $p < 2$ and that, for any such p, the error estimator is well defined and can be safely used.

The main goal of this paper is to solve an inverse problem corresponding to problem (2). More precisely, we consider this problem for a generic unknown dipole source $\boldsymbol{p}\,\delta_{\boldsymbol{x}_0}$; notice that both the polarization $\boldsymbol{p}$ and the localization $\boldsymbol{x}_0$ are unknown. To determine these two unknowns we have at our disposal a set of measured values of the solution to problem (2) at a certain number of fixed points on $\partial\Omega$. The aim of our inverse problem is to determine $\boldsymbol{p}$ and $\boldsymbol{x}_0$ such that the difference between the values of the solution of problem (2) and the corresponding measured values achieves a minimum in a proper way. The inverse problem is solved in an iterative fashion. At each step of the iteration it is necessary to solve the forward problem (2) for tentative values of the unknowns $\boldsymbol{p}$ and $\boldsymbol{x}_0$. Therefore, it is essential to have an efficient solver of this forward problem.

3. Forward problem

To prove existence and uniqueness of the solution, some regularity of $\boldsymbol{\sigma}$ in a vicinity of $\boldsymbol{x}_0$ has been assumed. From a physiological point of view, $\boldsymbol{\sigma}$ is regular

in each region of the head (scalp, skull and the different tissues of the brain) and $\boldsymbol{x}_0$ is located in the brain but typically close to the skull, where the conductivity is around eighty times smaller than the conductivity in the brain. After some experiments, we have seen that the subtraction approach is an excellent method when the dipole is located far enough from the interfaces, but it has an oscillating behavior when the dipole position lies closer and closer to the interface between two regions with different conductivities. We will show evidence of this fact below. We start describing the physical assumptions and the geometry where we will do the analysis. As shown in Figure 1 (left), the domain Ω is a multilayer square centered at $(0, 0)$; its dimensions are shown in the same figure. The conductivity $\boldsymbol{\sigma}$ is assumed isotropic on each layer and given by $\boldsymbol{\sigma}|_{\Omega_1} = \boldsymbol{\sigma}|_{\Omega_3} = 0.33$ and $\boldsymbol{\sigma}|_{\Omega_2} = 0.0042$. We will use these data in all the experiments.

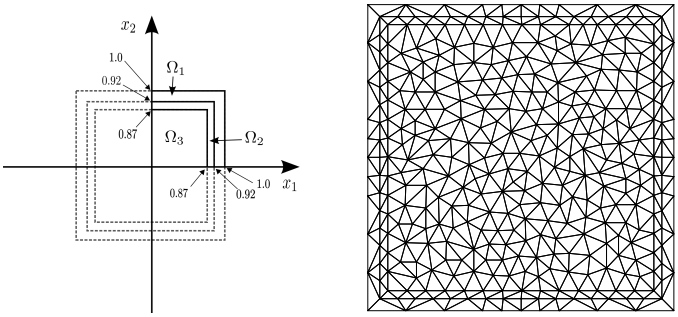

FIGURE 1. Domain Ω.

We will report a comparison between point values of the solutions obtained by using the direct approach with adaptivity (DAA) and the subtraction approach (SA) on uniformly refined meshes. Figure 1 (right) shows the coarsest used mesh in both cases. We have considered separately two locations for the point $\boldsymbol{x}_0 \in \Omega_3$, one far from the interface and the other one close. In both cases the unit vector $\boldsymbol{p} = (-0.2425, 0.9701)$ has been taken as polarization.

Figures 2 and 3 show the values of the solution at the point $(-0.75, 1)$, on the boundary, computed with SA and DAA. In Figure 2 we have taken the localization point $\boldsymbol{x}_0 = (0.012634, -0.004012)$ (far from the interface), whereas Figure 3 corresponds to $\boldsymbol{x}_0 = (0.012634, 0.86)$ (close to the interface). We see from Figure 2 that SA is stable in the case of $\boldsymbol{x}_0$ far from an interface, whereas DAA is a little bit oscillating at the coarser meshes, but stable in the finer. The situation is completely different when $\boldsymbol{x}_0$ is close to the interface, as can be seen from Figure 3 which shows that SA has a thoroughly unstable behavior on the coarser meshes, unlike DAA. Indeed, we observe that while the error on the initial mesh (shown in Figure 2, right) ranges between 1% and 5% for DAA, that for SA is below 1% when $\boldsymbol{x}_0$ is far from the interface (as in Figure 2), but is larger than 400% when $\boldsymbol{x}_0$ is close to it (as in Figure 3).

Let us remark that the point on the boundary $(-0.75, 1)$ has been chosen as for it the instability of SA on coarse meshes is clearly seen. However, the behavior shown in Figures 2 and 3 is qualitatively similar for all the points on the boundary. Thus, from our experimental information we may conclude that SA is not robust when $\boldsymbol{x}_0$ is located close to the interface. A theoretical analysis about this statement can be found in [22, Lemma 3.10]. On the contrary, DAA is fairly stable when the dipole position is in any region, near to or far from an interface. These conclusions

suggest that DAA could be a solution to fix this deficiency of SA. Anyway, we must not forget that when $\boldsymbol{x}_0$ is an internal point far from an interface, SA is a precise method, even better than DAA.

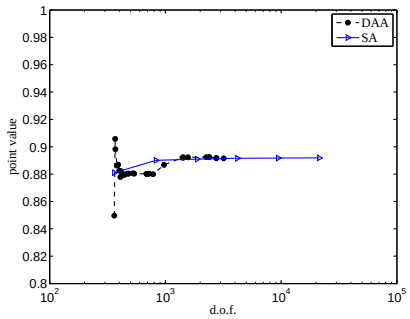

FIGURE 2. Forward problem. Point values of the solutions obtained by using SA and DAA with a dipole position $\boldsymbol{x}_0 = (0.012634, -0.004012)$ far from the interface.

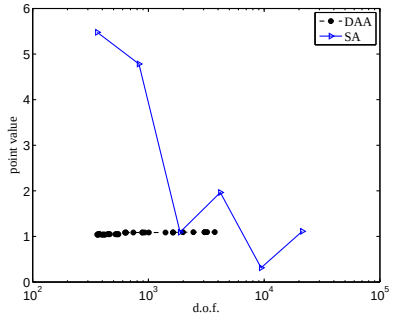

FIGURE 3. Forward problem. Point values of the solutions obtained by using SA and DAA with a dipole position $\boldsymbol{x}_0 = (0.012634, 0.86)$ close to the interface.

4. Inverse problem

In this section we discuss how to solve the inverse problem. Since we assume that the primary source to be determined is a single dipole, in principle we need to find four parameters $\boldsymbol{x} = (x_1, x_2)$ and $\boldsymbol{q} = (q_1, q_2)$ that minimize the objective function

$$\phi(\boldsymbol{x}, \boldsymbol{q}) := \|\boldsymbol{m}(\boldsymbol{x}, \boldsymbol{q}) - \boldsymbol{m}^{\text{meas}}\|_2^2, \quad \boldsymbol{x} \in \Omega,\ \boldsymbol{q} \in \mathbb{R}^2.$$

In the expression above

$$\boldsymbol{m}(\boldsymbol{x}, \boldsymbol{q}) := \begin{bmatrix} u(P_1) \\ \vdots \\ u(P_n) \end{bmatrix},$$

where $P_1, ..., P_n \in \partial\Omega$ are the observation points and u is the solution to problem (7) with polarization $\boldsymbol{q}$ and localization $\boldsymbol{x}$, namely, $u \in L^p(\Omega)$ is such that

$$\begin{cases} \displaystyle\int_\Omega u \ \mathrm{div}(\boldsymbol{\sigma}\,\nabla\varphi) = -\boldsymbol{q}\cdot\nabla\varphi(\boldsymbol{x}) & \forall\,\varphi \in X\,, \\ \displaystyle\int_\Omega u = 0\,. \end{cases} \tag{11}$$

In its turn,

$$\boldsymbol{m}^{\mathrm{meas}} := \begin{bmatrix} u^{\mathrm{meas}}(P_1) \\ \vdots \\ u^{\mathrm{meas}}(P_n) \end{bmatrix}$$

is the vector of corresponding measured values at the same points $P_1, ..., P_n$.

For each $\boldsymbol{x} \in \Omega$ we can determine the optimal polarization $\boldsymbol{p_x}$ as follows: if we write $\boldsymbol{q} = q_1\mathbf{e}_1 + q_2\mathbf{e}_2$, where $\mathbf{e}_1$ and $\mathbf{e}_2$ are the Cartesian unit vectors, then, being problem (11) linear with respect to the polarization, we can decompose

$$\boldsymbol{m}(\boldsymbol{x}, \boldsymbol{q}) = q_1\boldsymbol{m}(\boldsymbol{x}, \mathbf{e}_1) + q_2\boldsymbol{m}(\boldsymbol{x}, \mathbf{e}_2) = \boldsymbol{M}(\boldsymbol{x})\boldsymbol{q},$$

where $\boldsymbol{M}(\boldsymbol{x})$ is the $n \times 2$ matrix

$$\begin{bmatrix} \boldsymbol{m}(\boldsymbol{x}, \mathbf{e}_1) & \boldsymbol{m}(\boldsymbol{x}, \mathbf{e}_2) \end{bmatrix}.$$

Thus, given $\boldsymbol{x} \in \Omega$, to find $\boldsymbol{p_x} = \boldsymbol{q} \in \mathbb{R}^2$ that minimizes $\phi(\boldsymbol{x}, \boldsymbol{q}) = \|\boldsymbol{M}(\boldsymbol{x})\boldsymbol{q} - \boldsymbol{m}^{\mathrm{meas}}\|_2^2$ is equivalent to determining the solution $\boldsymbol{p_x}$ of the normal equations, namely, solving the 2×2 system

$$\boldsymbol{M}^t(\boldsymbol{x})\boldsymbol{M}(\boldsymbol{x})\boldsymbol{p_x} = \boldsymbol{M}^t(\boldsymbol{x})\boldsymbol{m}^{\mathrm{meas}}\,. \tag{12}$$

Therefore, the objective function ϕ reduces to a function ψ only of $\boldsymbol{x}$:

$$\psi(\boldsymbol{x}) := \|\boldsymbol{M}(\boldsymbol{x})\boldsymbol{p_x} - \boldsymbol{m}^{\mathrm{meas}}\|_2^2\,, \tag{13}$$

$\boldsymbol{p_x}$ being the solution of (12). The next step is to choose an efficient optimization algorithm for this function.

4.1. Minimization algorithm. To find the optimal dipole position, we need to choose an optimization method. With this aim, we start analyzing the objective function ψ to determine the possible existence of local minima. With this purpose we have computed the objective function in a particular case. We have chosen $\boldsymbol{x}_0 = (0.012634, 0.8696)$ and $\boldsymbol{p} = (-0.2425, 0.9701)$ and computed very accurately "measured" values $\boldsymbol{m}^{\mathrm{meas}} = (u^{\mathrm{meas}}(P_1), ..., u^{\mathrm{meas}}(P_{30}))$ with $P_1, ..., P_{30}$ as shown in Figure 4.

Then, we have evaluated the objective function $\psi(\boldsymbol{x})$ with u computed by means of the direct approach on the mesh shown in Figure 5. Let us recall that this approach leads to constant values of u on each triangle of the mesh and, consequently, also to constant values of ψ.

Figure 5 shows the objective function ψ. It is possible to appreciate in the figure the existence of local minima, although in Ω_1. Because of physiological reasons, we are interested in solving the inverse problem for $\boldsymbol{x}$ in the most internal region of the geometry, Ω_3 (which corresponds to the brain), where in this case there are not local minima.

We have chosen the simulated annealing algorithm which is an excellent optimization method to solve the inverse problem, specially in presence of local minima.

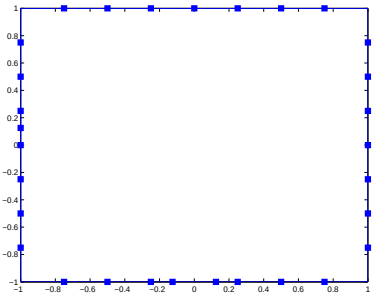

FIGURE 4. Observation points on the boundary.

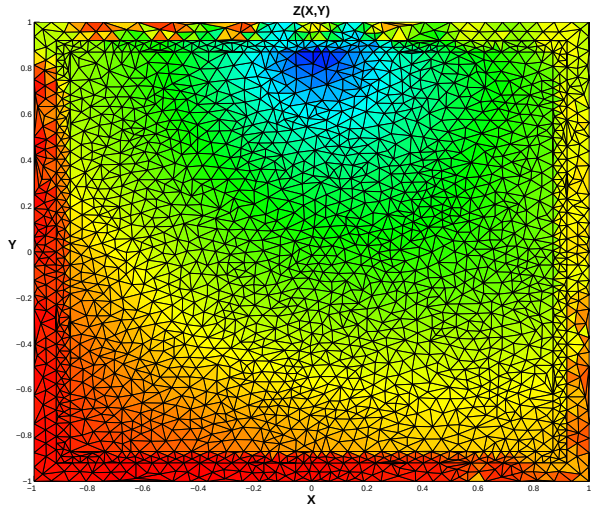

FIGURE 5. Objective function evaluated in the triangles of the mesh.

This method is a probabilistic algorithm based on an analogy to the thermodynamic process known as annealing, consisting of the slow cooling of a substance from a liquid to a solid state. In our code, we use the MATLAB command `simulannealbnd`, which corresponds to this method. Moreover, since in practice the localization $\boldsymbol{x}_0$ necessarily lies in Ω_3 (brain), we constrain the optimization to values of $\boldsymbol{x}$ in this subdomain.

4.2. Adaptive strategy of minimization. The main goal of this paper is to compare the performances of the direct approach and SA to solve the inverse problem. In the case of the former, as described above, the objective function takes constant values on each triangle of the mesh. Therefore, for an accurate determination of $\boldsymbol{x}_0$, it is necessary to use meshes properly refined in the vicinity of this (unknown) point. Moreover, the solution to the underlying forward problem (11) presents a strong singularity at $\boldsymbol{x}$, which makes necessary to use meshes highly refined around this (varying) point. Given $\boldsymbol{x}$, such refined meshes can be obtained

TABLE 1. Algorithm of minimization.

Algorithm 1 Adaptive strategy of minimization
DATA: an initial coarse mesh$\mathcal{T}_h^0$ and a randomly chosen $\boldsymbol{x}_0^{(0)}$;
1: **for** $k = 0, 1, 2, ...$
2: `simulannealbnd`($\mathcal{T}_h^k$,$\boldsymbol{x}_0^{(k)}$), **OUTPUT**: $\boldsymbol{x}_0^{(k+1)}$;
3: four steps of adaptive refinement process, **OUTPUT**: $\mathcal{T}_h^{k+1}$;
4: **until the stopping criterion is reached.**

by using the a posteriori error indicator $\eta_{T,p}$ (cf. (10)). We will only report the results of the tests made with $p = 1.25$. However, the conclusions of our analysis are independent of the chosen value of p. On the other hand, let us remark that the location of $\boldsymbol{x}$ changes through the minimization process. Therefore, we need to derive a strategy that combines both processes, the minimization and the mesh refinement.

With this aim, we designed an algorithm to solve the inverse problem that consists in the following: first, we use an initial coarse mesh $\mathcal{T}_h^0$ and a randomly chosen $\boldsymbol{x}_0^{(0)}$. Then, we enter in a loop which has as stopping criterion that the objective function decreases below a certain threshold. Within this loop, the first step is to minimize the objective function ψ computed by direct approach, by using the command `simulannealbnd` which receives as input: $\mathcal{T}_h^0$ and $\boldsymbol{x}_0^{(0)}$. As output we obtain a new approximation of the localization, $\boldsymbol{x}_0^{(1)}$, that we use to compute the corresponding polarization $\boldsymbol{p}_{x_0}^{(1)}$ by solving (12). Next, we perform four steps of the adaptive refinement process to solve problem (11) with right hand side $-\boldsymbol{p}_{\boldsymbol{x}_0}^{(1)} \cdot \nabla\varphi(\boldsymbol{x}_0^{(1)})$, the final mesh $\mathcal{T}_h^1$ being the output of this stage. Then, we perform a new minimization step by using now $\boldsymbol{x}_0^{(1)}$ and $\mathcal{T}_h^1$ instead of $\boldsymbol{x}_0^{(0)}$ and $\mathcal{T}_h^0$. We continue with the process until the stopping criteria is reached. The algorithm is summarized in Table 4.2.

The reason for the random choice of $\boldsymbol{x}_0^{(0)}$ is to avoid using any a priori information about the location of the dipole source. In practice, if such a priori information were available, it could be used to speed up the process. However, even for a random choice, we have always observed convergence of the above algorithm.

Let us recall that the accuracy of direct approach to solve the inverse problem is limited by the meshsize of the triangle containing the dipole location $\boldsymbol{x}_0^{(k+1)}$. In fact, the values at the observation points computed with direct approach only depend on which is the triangle T_0 containing $\boldsymbol{x}_0^{(k+1)}$, but not on the position of $\boldsymbol{x}_0^{(k+1)}$ in T_0 (see Remark 2.2). Thus, in this case, we will take as $\boldsymbol{x}_0^{(k+1)}$ the barycenter of this triangle T_0.

5. Simulation of measurements

To solve the inverse problem, it is necessary to know the measured values $\boldsymbol{m}^{\text{meas}} = (u^{\text{meas}}(P_1), ..., u^{\text{meas}}(P_n))$ at the observation points $P_1, ..., P_n$. In practice, these values are actually measured through EEG. In the following section we will simulate this process in order to compare the performances of DAA and SA. To do this, we need to have at our disposal accurately simulated "measured" values. Since we do not have an analytical solution of the forward problem, we will use numerical methods on extremely fine meshes to obtain these "measurements". In this section we will discuss which methods can be safely used to simulate these "measurements",

depending of the localization of $\boldsymbol{x}_0$. We will focus in determining the "measurements" in three cases: with the dipole position in Ω_3, far, close and very close to the interface with Ω_2. More precisely, in our case in which the domain is a square of the order of the unit, we have taken the dipole position separated from the closest interface 0.6285 (far), 0.01 (close) and 0.0004 (very close). In all cases, we consider the thirty observation points shown in Figure 4.

In the case that the dipole position is a point far from an interface, we know that it is possible to solve the forward problem very accurately with the SA using FEM on a very fine mesh. However, we need to determine the number of decimal digits that are reliable. To this end, we also computed the "measured" values by using DAA and we compared both results.

First, we consider the dipole position $\boldsymbol{x}_0 = (0.15231, 0.24150)$ and polarization, $\boldsymbol{p} = (-0.2425, 0.9701)$. For SA, we used a sequence of twelve successively refined uniform meshes, where the coarser one contains 362 d.o.f and the finer 2,923,631 d.o.f. In Table 2 we report values of the solution at five of the observation points computed with SA on some of these meshes. We observe that the computed values clearly converge for each observation point and that at least four decimal digits are reliable. This table is a sample of what happens with any of the thirty points and all the meshes.

TABLE 2. Convergence for SA when $\boldsymbol{x}_0 = (0.15231, 0.24150)$ is far from the interface.

	Observation points				
d.o.f.	(-1, -0.75)	(-1, 0.5)	(-0.75, 1)	(0, 1)	(1, 0.25)
1,879	0.01274	0.68858	0.96247	1.17484	0.21499
4,180	0.01368	0.68837	0.96369	1.17566	0.21467
21,338	0.01455	0.68812	0.96463	1.17634	0.21444
110,528	0.01485	0.68807	0.96491	1.17659	0.21438
569,434	0.01494	0.68805	0.96499	1.17665	0.21436
1,290,999	0.01496	0.68805	0.96500	1.17667	0.21436
"Exact" values	0.0150	0.6881	0.9650	1.1767	0.2144

Although in this case SA leads to a reliable determination of the "measurements", we also computed them with DAA. We report in Figure 6 error curves (the Euclidean norm of the vector of errors at all the observation points for both methods). To compute the plotted errors, we have taken as "exact" values those obtained with SA on an extremely fine mesh (2,923,631 d.o.f.).

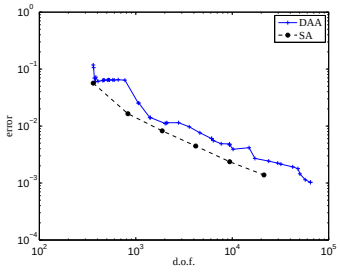

FIGURE 6. Error curves for SA and DAA when $\boldsymbol{x}_0 = (0.15231, 0.24150)$ is far from the interface.

We can see from Figure 6 that, in this case, SA exhibits a better performance than DAA, although the latter converges to the same values. By repeating several

times this experiment, we conclude that such a behavior is typical for any dipole localization $\boldsymbol{x}_0$ far from the interfaces. However, we will show below that this is not the case when $\boldsymbol{x}_0$ is close to an interface.

Secondly, we considered as dipole localization $\boldsymbol{x}_0 = (0.012634, 0.86)$. Notice that this point is at a distance 0.01 from the interface. We repeated the procedure described above. We include in Table 3 and Figure 7 the corresponding information. We also report in Table 3 the values computed with DAA.

TABLE 3. Convergence for SA and DAA when $\boldsymbol{x}_0 = (0.012634, 0.86)$ is close to the interface.

		Observation points				
Method	d.o.f.	(-1, -0.75)	(-1, 0.5)	(-0.75, 1)	(0, 1)	(1, 0.25)
SA	1,879	0.30696	0.69807	1.09337	1.80180	-0.00942
	4,180	0.11748	0.85576	1.96375	5.46707	0.10636
	21,338	0.18911	0.59929	1.11234	2.43831	0.02676
	110,528	0.19220	0.59723	1.10051	2.38082	0.02512
	569,434	0.19210	0.59738	1.10157	2.38411	0.02521
	1,290,999	0.19210	0.59735	1.10156	2.38439	0.02521
DAA	1,637	0.19101	0.59649	1.08818	2.37749	0.02467
	3,745	0.19124	0.59589	1.09465	2.38222	0.02491
	25,141	0.19185	0.59711	1.10004	2.38397	0.02501
	116,299	0.19204	0.59731	1.10126	2.38418	0.02519
	156,175	0.19205	0.59731	1.10137	2.38419	0.02520
"Exact" values		0.1921	0.5974	1.1016	2.3843	0.0252

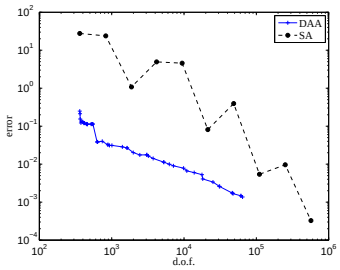

FIGURE 7. Error curves for SA and DAA when $\boldsymbol{x}_0 = (0.012634, 0.86)$ is close to the interface.

It can be clearly seen from Figure 7 and Table 3 that SA yields very inaccurate computations in this case for the coarser meshes. Indeed, the computed values are not close to the "exact" ones until the number of degrees of freedom is larger than $20,000$ which, for a two-dimensional test like this, corresponds to a highly refined mesh. According to our experiments, it is typical of SA that it yields accurate results only when the mesh size is smaller than the distance from $\boldsymbol{x}_0$ to the interface. Thus, SA becomes fairly stable only for sufficiently fine meshes. Instead, DAA yields accurate values even for the coarsest meshes. Moreover, the behavior of this approach looks much more stable.

Finally, we considered a dipole localization extremely close to the interface: $\boldsymbol{x}_0 = (0.012634, 0.8696)$, which is at a distance 0.0004. Let us remark that it is not rare in EEG that the primary current occurs practically on the interfaces, so that to consider such an $\boldsymbol{x}_0$ makes perfect sense. We repeated once more the same procedure and report the computed values in Table 4 and the corresponding error curves in Figure 8.

It can be clearly seen that, in this case, SA fails completely to converge. Such a behavior agrees with what was observed in the previous case: SA yields accurate

results only if the meshsize is smaller than the distance from $\boldsymbol{x}_0$ to the interface. Notice that, in this case, we would need a mesh with more that 10^9 d.o.f. for attaining such a threshold (in spite of the two-dimensional character of the test).

In order to have an alternative to double check the values computed with DAA, we have also used in this case a hybrid approach: we have solved the problem with SA on the meshes adaptively created with the direct approach. Although the error indicator used to create these meshes depends on the error of the direct approach, it leads to meshes highly refined in the vicinity of $\boldsymbol{x}_0$. Therefore, the threshold of SA is attained at least in this vicinity. We labelled the results obtained with this hybrid procedure as SAA (subtraction approach with adaptivity). We include these results in Table 4 and Figure 8 in which a very accurate agreement between SAA and DAA can be seen. Let us remark that this agreement supports the possibility of designing a proper error estimate for SA to drive an adaptive scheme based on this method. Although we will not pursue this approach in this paper, it will be the subject of some future research.

TABLE 4. Convergence for SA, SAA and DAA when $\boldsymbol{x}_0 = (0.012634, 0.8696)$ is very close to the interface.

		Observation points				
Method	d.o.f.	(-1, -0.75)	(-1, 0.5)	(-0.75, 1)	(0, 1)	(1, 0.25)
SA	1,879	-2.70522	6.36421	23.29707	85.52184	2.36181
	4,180	-0.04099	1.58093	4.23547	13.82857	0.33094
	21,338	-3.04040	4.76241	20.30180	76.39359	2.16830
	110,528	-0.61454	1.97822	6.84558	23.71393	0.61727
	569,434	-0.36542	1.45897	4.82940	16.42804	0.41847
	1,290,999	-0.06074	0.84485	2.41737	7.66346	0.17806
SAA	1,386	0.18985	0.60796	1.14112	2.65156	0.02691
	4,510	0.19369	0.59594	1.10786	2.50092	0.02344
	26,184	0.19663	0.59314	1.09734	2.44863	0.02228
	105,992	0.19680	0.59334	1.09820	2.44730	0.02238
	186,197	0.19681	0.59332	1.09826	2.44717	0.02238
DAA	1,386	0.19574	0.59222	1.08442	2.43143	0.02186
	4,510	0.19575	0.59272	1.09336	2.44287	0.02240
	26,184	0.19669	0.59306	1.09695	2.44579	0.02227
	105,992	0.19681	0.59332	1.09810	2.44674	0.02237
	186,197	0.19681	0.59333	1.09825	2.44685	0.02239
"Exact" values		0.1968	0.5933	1.0983	2.4472	0.0224

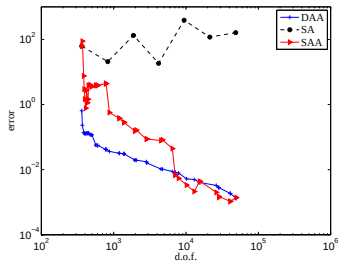

FIGURE 8. Error curves for SA, SAA and DAA when $\boldsymbol{x}_0 = (0.012634, 0.8696)$ is very close to the interface.

6. Numerical experiments

In this section, we focus on the inverse problem and compare the two strategies, SA and DAA. To this end, we consider the same geometry and assess the performance of each strategy depending on how close the dipole location is to an

interface. We will show that also for the inverse problem both approaches behaves similarly when the dipole is located far enough from an interface, but that DAA is clearly preferable when the dipole is close to an interface. Finally, we will discuss the robustness of DAA with respect to measurements errors.

6.1. Test 1. This experiment consists in reconstructing the position and the polarization of the dipole source from boundary measurements by using the aforementioned methods when the dipole location in Ω_3 is far from the interface. We considered in this test $\boldsymbol{x}_0 = (0.15231, 0.24150)$ as dipole position and the same polarization used in all the other cases: $\boldsymbol{p} = (-0.2425, 0.9701)$.

We define the percentage errors $\mathbf{e}(\boldsymbol{x})$ and $\mathbf{e}(\boldsymbol{p}_{\boldsymbol{x}})$ as follows:

$$\mathbf{e}(\boldsymbol{x}) := 100\frac{\|\boldsymbol{x}_0 - \boldsymbol{x}\|_2}{\|\boldsymbol{x}_0\|_2} \qquad \text{and} \qquad \mathbf{e}(\boldsymbol{p}_{\boldsymbol{x}}) := 100\frac{\|\boldsymbol{p} - \boldsymbol{p}_x\|_2}{\|\boldsymbol{p}\|_2},$$

where $\boldsymbol{x}$ and $\boldsymbol{p}_{\boldsymbol{x}}$ correspond to the approximations of $\boldsymbol{x}_0$ and $\boldsymbol{p}$ obtained by solving the inverse problem.

In Table 5 we report the localization and polarization obtained by solving the inverse problem by using SA in four different uniform meshes as well as the corresponding percentage errors. We also include columns with the number of d.o.f., the value of the objective function ψ to be minimized and the CPU time for each mesh. Finally, we include the exact values $\boldsymbol{x}_0$ and $\boldsymbol{p}$ in the last row of the table.

TABLE 5. Test 1. Results obtained by solving the inverse problem with SA: localization, polarization, percentage errors, objective function and CPU time (in seconds).

d.o.f.	$\boldsymbol{x}$	$\mathbf{e}(\boldsymbol{x})$	$\boldsymbol{p}_{\boldsymbol{x}}$	$\mathbf{e}(\boldsymbol{p}_{\boldsymbol{x}})$	$\psi(\boldsymbol{x})$	CPU time
362	(0.1524, 0.2509)	3.30	(-0.2437, 0.9784)	0.83	0.040	19.37
829	(0.1520, 0.2453)	1.33	(-0.2426, 0.9718)	0.17	0.012	37.78
1,879	(0.1524, 0.2431)	0.58	(-0.2426, 0.9710)	0.08	0.006	48.69
4,180	(0.1519, 0.2427)	0.45	(-0.2425, 0.9706)	0.04	0.003	185.13
Exact	(0.1523, 0.2415)	-	(-0.2425, 0.9701)	-	-	-

On the other hand, in Table 6.1 we present the same information for several iterations of DAA, which allows us to see the evolution of this process. The behavior of each strategy can be better appreciated in Figures 9 and 10, which show log-log plots of the errors $\mathbf{e}(\boldsymbol{x})$ and $\mathbf{e}(\boldsymbol{p}_{\boldsymbol{x}})$, respectively. We observe from these two figures that both strategies lead to very accurate results, SA being more stable than DAA, which presents a less monotonic behavior. On the other hand, it can be seen in Tables 5 and 6.1 that in this case SA is less expensive.

TABLE 6. Test 1. Results obtained by solving the inverse problem with DAA: localization, polarization, percentage errors, objective function and CPU time (in seconds).

Iteration	d.o.f.	$\boldsymbol{x}$	$\mathbf{e}(\boldsymbol{x})$	$\boldsymbol{p}_{\boldsymbol{x}}$	$\mathbf{e}(\boldsymbol{p}_{\boldsymbol{x}})$	$\psi(\boldsymbol{x})$	CPU time
1	362	(0.1623, 0.2513)	4.90	(-0.2318, 0.9780)	1.33	0.101	8.36
5	595	(0.1508, 0.2535)	4.25	(-0.2436, 0.9789)	0.88	0.048	71.86
10	1,847	(0.1509, 0.2442)	1.07	(-0.2418, 0.9711)	0.11	0.016	203.30
15	4,380	(0.1518, 0.2425)	0.39	(-0.2423, 0.9697)	0.05	0.008	520.08
Exact		(0.1523, 0.2415)	-	(-0.2425, 0.9701)	-	-	-

Figure 11 shows some of the successively refined meshes created in the process driven by DAA. Figure 12 shows two zooms around the singularity of the finer mesh in Figure 11. The second figure is a 200% zoom and the third one is an 800% zoom of the first one. In the last figure the evidence of the process of search generated by

DAA can be appreciated by the location of the points around which the adaptive process leads to refinement.

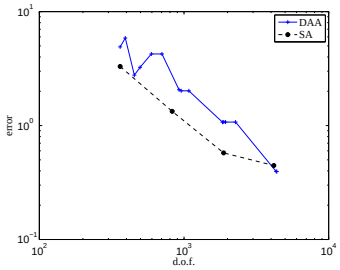

FIGURE 9. Test 1. Percentage error curves for the localization $\boldsymbol{x}_0$ of the solution of the inverse problem by using SA and DAA.

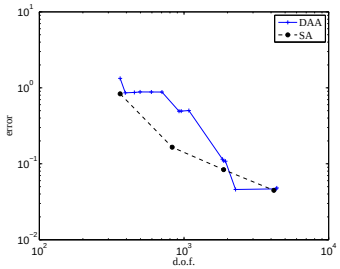

FIGURE 10. Test 1. Percentage error curves for the polarization $\boldsymbol{p}$ of the solution of the inverse problem by using SA and DAA.

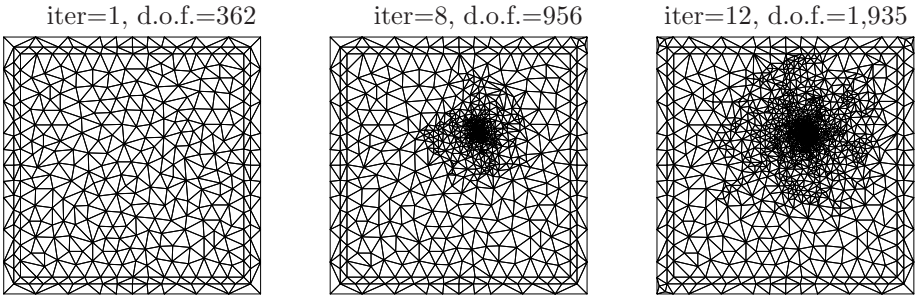

FIGURE 11. Test 1. Meshes obtained in the process driven by DAA.

6.2. Test 2. This experiment is totally similar to Test 1. The only difference is the position of the dipole source in Ω_3, which now is taken very close to the interface with Ω_2. We used the same dipole position as in Section 4: $\boldsymbol{x}_0 = (0.012634\,, 0.8696)$. The polarization is the same as in the experiment above: $\boldsymbol{p} = (-0.2425, 0.9701)$.

We report in Tables 7 and 8 and Figures 13 and 14 the same information as in the previous test. In this case, it can be clearly seen that the performance of DAA is significantly better than that of SA. In fact, for the latter, no convergence can

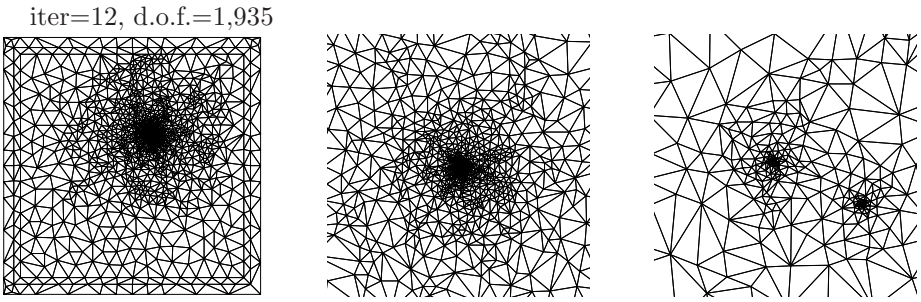

FIGURE 12. Test 1. Meshes obtained in the process driven by DAA. Successive zooms of the mesh for iter=13.

be appreciated for the polarization $\boldsymbol{p}$. In its turn the location $\boldsymbol{x}_0$ can be computed with a percentage error of around 1% on a rather coarse mesh, although this cannot be improved with finer meshes. Instead DAA behaves in a much more stable way and allows us to compute both $\boldsymbol{x}_0$ and $\boldsymbol{p}$ with significantly smaller errors.

Figure 15 shows a zoom of the domain in which we report some successive positions and polarizations obtained by means of DAA. We also include the exact $\boldsymbol{x}_0$ and $\boldsymbol{p}$. The number nearby each point corresponds to the iteration number. Let us remark that the errors of all the localization shown in this zoom are smaller than 2.5%.

As a consequence of these two tests we can assert that DAA is clearly preferable when the dipole is located close to an interface. Moreover, in such a case SA even fails to converge. On the other hand, when the dipole is far from an interface, although SA exhibits a better performance, DAA is fairly stable and leads to competitive results.

TABLE 7. Test 2. Results obtained by solving the inverse problem with SA: localization, polarization, percentage errors, objective function and CPU time (in seconds).

d.o.f.	$\boldsymbol{x}$	$\mathbf{e}(\boldsymbol{x})$	$\boldsymbol{p}_{\boldsymbol{x}}$	$\mathbf{e}(\boldsymbol{p}_{\boldsymbol{x}})$	$\psi(\boldsymbol{x})$	CPU time
362	(0.0186, 0.8518)	2.16	(-0.2531, -0.0219)	99.21	0.0720	30.84
829	(0.0679, 0.8673)	6.36	(1.1304, 0.4758)	145.92	0.0236	25.20
1,879	(0.0138, 0.8632)	0.75	(-0.1624, 0.4771)	49.95	0.0092	54.62
4,180	(0.0114, 0.8633)	0.74	(-0.2537, -0.0720)	104.22	0.0104	104.04
9,417	(0.0096, 0.8645)	0.68	(-0.2310, 0.0169)	104.22	0.0040	479.41
Exact	(0.0126, 0.8696)	-	(-0.2425, 0.9701)	-	-	-

TABLE 8. Test 2. Results obtained by solving the inverse problem with DAA: localization, polarization, percentage errors, objective function and CPU time (in seconds).

Iter.	d.o.f.	$\boldsymbol{x}$	$\mathbf{e}(\boldsymbol{x})$	$\boldsymbol{p}_{\boldsymbol{x}}$	$\mathbf{e}(\boldsymbol{p}_{\boldsymbol{x}})$	$\psi(\boldsymbol{x})$	CPU time
1	362	(0.0210, 0.7915)	9.03	(-0.2585, 1.0222)	5.44	0.213	8.52
5	521	(-0.0007, 0.8644)	1.64	(-0.2464, 0.9953)	2.55	0.081	53.77
10	1,013	(0.0132, 0.8676)	0.24	(-0.2430, 0.9817)	1.16	0.020	146.60
Exact		(0.0126, 0.8696)	-	(-0.2425, 0.9701)	-	-	-

6.3. Test 3. We must have in mind that, in problems like this, the measurements are always affected by errors. For this reason, it is important to analyze the robustness of the proposed method when the data is subjected to noise. With this

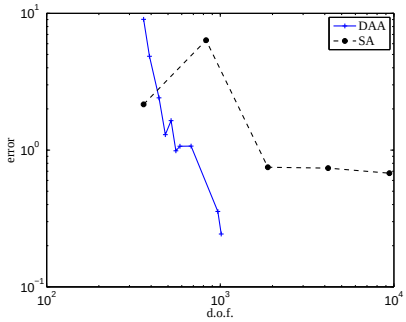

FIGURE 13. Test 2. Percentage error curves for the localization $\boldsymbol{x}_0$ of the solution of the inverse problem by using SA and DAA.

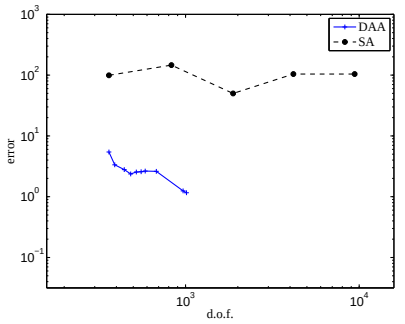

FIGURE 14. Test 2. Percentage error curves for the polarization $\boldsymbol{p}$ of the solution of the inverse problem by using SA and DAA.

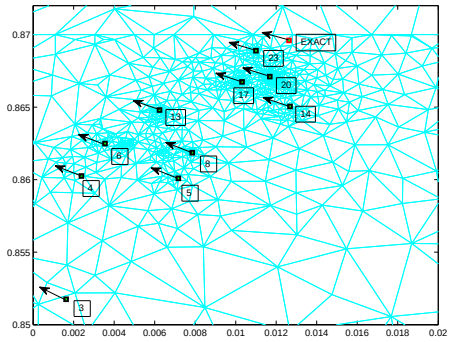

FIGURE 15. Test 2. Some of the successive positions and polarizations obtained by means of DAA.

aim, we have repeated the experiment of Test 2, but with the measurements perturbed by uniformly distributed errors with a maximum size of 5% of the maximum value of the data (let us remark that this amounts to an average relative error of around 10%). We report the obtained results in Table 9. We observe that these

measurement errors produce percentage errors of 1.83% and 3.67% in the determination of the localization $\boldsymbol{x}_0$ and the polarization $\boldsymbol{p}$, respectively, on the finer meshes obtained with DAA.

TABLE 9. Test 3. Results obtained by solving the inverse problem with DAA using perturbed measurements with 5% maximum error size.

Iter.	d.o.f.	$\boldsymbol{x}$	$\boldsymbol{p}_{\boldsymbol{x}}$	$\mathbf{e}(\boldsymbol{x})$	$\mathbf{e}(\boldsymbol{p}_{\boldsymbol{x}})$
1	362	(0.0210, 0.7915)	(-0.2881, 0.9963)	9.03	5.26
5	511	(0.0242, 0.8538)	(-0.2818, 0.9752)	2.25	3.96
10	1,222	(0.0225, 0.8572)	(-0.2784, 0.9624)	1.83	3.67
Exact		(0.0126, 0.8696)	(-0.2425, 0.9701)	-	-

In order to study how the method depends on the size of the measurement errors, we have repeated the previous experiment using different maximum error sizes: 1%, 5% and 10% of the maximum value of the measurements. We plot all the error curves for $\boldsymbol{x}_0$ on Figure 16 and for $\boldsymbol{p}$ on Figure 17. To allow for comparison, the figures also include the data "0%" corresponding to the problem without measurement errors. Finally, Table 10 shows the percentage error in the determination of $\boldsymbol{x}_0$ and $\boldsymbol{p}$ on the finest mesh for the different maximum error sizes.

Let us remark that, in all cases, DAA converges. However, in presence of measurements data errors, it converges to 'wrong' $\boldsymbol{x}_0$ and $\boldsymbol{p}$; namely, it converges to the correct values of $\boldsymbol{x}_0$ and $\boldsymbol{p}$ that are exact solution for the perturbed data. For instance, it can be seen that when the maximum percentage data error is 5%, the adaptive process converges to values of $\boldsymbol{x}_0$ and $\boldsymbol{p}$ with respective errors of 1.83% and 3.67% according to Table 10. This is the reason why the corresponding error curves in Figures 16 and 17 stall at these percentages.

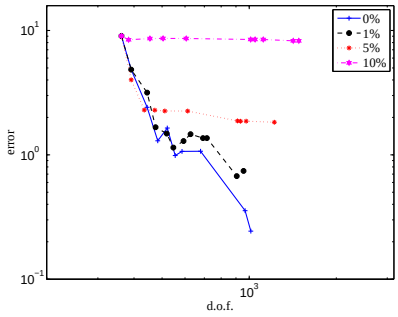

FIGURE 16. Test 3. Comparison between percentage error curves for the localization $\boldsymbol{x}_0$ obtained by solving the inverse problem with DAA using perturbed measurements with different maximum error size.

7. Conclusions

We have analyzed two approximation methods for the inverse problem of electroencephalography: subtraction approach (SA) on uniform meshes and direct approach with adaptivity (DAA). The study was done in a 2D framework, but the conclusions should remain valid for 3D problems as well, the only challenge being the significantly larger computational cost.

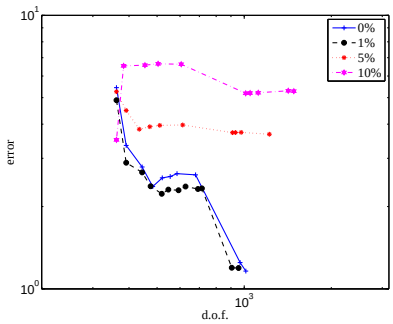

FIGURE 17. Test 3. Comparison between percentage error curves for the polarization $\boldsymbol{p}$ obtained by solving the inverse problem with DAA using perturbed measurements with different maximum error sizes.

TABLE 10. Test 3. Percentage errors in the determination of $\boldsymbol{x}_0$ and $\boldsymbol{p}$ on the finest mesh computed with DAA using perturbed measurements with different maximum error size.

Measurement errors	0%	1%	5%	10%
$\boldsymbol{x}_0$ error	0.24%	0.74%	1.83%	8.26%
$\boldsymbol{p}$ error	1.16%	1.19%	3.67%	5.28%

We observed in the forward problem that both strategies are stable when the dipole position is sufficiently far from an interface. However, when the dipole is close to an interface, SA may yield unstable solutions. Instead, DAA does not exhibit such a behavior. Therefore, we presume that the latter is a better candidate to be used for solving the inverse problem.

From the experimental evidence we conclude that both methods yield accurate results for the inverse problem when the dipole is far from the interfaces. Instead, when the dipole is close to an interface, SA leads to reasonable results with respect to the dipole position only for sufficiently fine meshes, whereas in all the numerical experiments the approximation of the polarization is quite inaccurate. In the case of DAA the approximation of both, location and polarization are thoroughly satisfactory. Finally, our experimental results allow us to conclude that DAA is a robust strategy with respect to measurement errors to solve the inverse problem, too.

The main advantage of DAA with respect to SA is the fact that it uses adaptively created meshes that are appropriate to deal with the singular character of the solution. Our preliminary experiments seem to show that adaptively refined meshes could be useful for SA too [20]. This fact opens the possibility of designing an error indicator for SA and creating an adaptive scheme based on this approach, which will be a subject of future research.

Acknowledgements. The first and fourth authors have been partially supported by GNCS-INdAM. The second author was partially supported by a CONICYT, Becas Chile fellowship (Chile), by Centro de Investigación en Ingeniería Matemática (CI^{2}MA), Universidad de Concepción, through the BASAL project CMM, Universidad de Chile; CONICYT (Chile) through project Inserción de Capital Humano Avanzado en la Academia 79130048 and by project FONDECYT 11140691. The

third author was partially supported by BASAL project, CMM, Universidad de Chile and Anillo ANANUM, ACT1118, CONICYT (Chile).

References

[1] Albanese, R. and Monk, P.B. The inverse source problem for Maxwell's equations. Inverse Problems. 22(3):1023–1035, 2006.

[2] Alonso-Rodríguez, A., Camaño, J. and Valli, A. Inverse source problems for eddy current equations. Inverse Problems. 28(1):15006–15015, 2012.

[3] Alonso-Rodríguez, A., Camaño, J., Rodríguez, R. and Valli, A. A posteriori error estimates for the problem of electrostatics with a dipole source. *Preprint DIM 2013-07.* Universidad de Concepción, Concepción, Chile, 2013.

[4] Ammari, H., Bao, G. and Fleming, J.L. An inverse source problem for Maxwell's equations in magnetoencephalography. SIAM J. Appl. Math. 62(4):1369–1382, 2002.

[5] Awada, K.A., Jackson, D.R., Williams, J.T., Wilton, D.R., Baumann, S.B. and Papanicolaou, A.C. Computational aspects of finite element modeling in EEG source localization. IEEE Trans Biomed Eng. 44(8):736–752, 1997.

[6] Bertrand, O., Thévenet, M. and Perrin, F. 3D finite element method in brain electrical activity studies, in *Biomagnetic Localization and 3D Modeling,* J. Nenonen, H. M. Rajala and T. Katila, eds., Tech. rep., Department of Technical Physics, Helsinki University of Technology, Otaniem, Finland, 154–171, 1991.

[7] Ciarlet, P.G. *The Finite Element Method for Elliptic Problems.* North-Holland, Amsterdam 1978.

[8] Dassios, G. and Hadjiloizi, D. On the non-uniqueness of the inverse problem associated with electroencephalography. Inverse Problems. 25(11):115012–115018, 2009.

[9] De Munck, J.C., Wolters, C.H. and Clerc, M. EEG and MEG: forward modeling, in *Handbook of neural activity measurement.* Cambridge Univ. Press, Cambridge, 192–256, 2012.

[10] El Badia, A. and Nara, T. An inverse source problem for quasi-static Maxwell's equations. J. Inverse Ill-Posed Probl. 18(7):741–764, 2010.

[11] He, S. and Romanov, V.G. Identification of dipole sources in a bounded domain for Maxwell's equations. Wave Motion 28(1):25–40, 1998.

[12] Lew, S., Wolters, C.H., Dierkes, T., Röer, C. and MacLeod, R.S. Accuracy and run-time comparison for differential potential approaches and iterative solvers in finite element method based EEG source analysis. Appl. Numer. Math. 59(8):1970–1988, 2009.

[13] Niedermeyer, E. and Lopes da Silva, F. *Electroencephalography: Basic Principles, Clinical Applications, and Related Fields* Fifth Edition. Philadelphia, PA: Williams & Wilkins 2004.

[14] Sarvas, J. Basic mathematical and electromagnetic concepts of the biomagnetic inverse problem. Physics in Medicine and Biology. 32(1):11–22, 1987.

[15] Sauter, S.A. and Schwab, C. Boundary element methods. Springer-Verlag, Berlin, 2011.

[16] Schimpf, P.H., Ramon, C.R. and Haueisen, J. Dipole models for the EEG and MEG. IEE Trans. Biomed. Engrg., 49:409–418, 2002.

[17] Plonsey, R. and Heppner, D. Considerations of quasi-stationarity in electrophysiological systems. Bull. Math. Biophys. 29:657–664, 1967.

[18] Valli, A. Solving an electrostatics-like problem with a current dipole source by means of the duality method. Appl. Math. Lett. 25(10):1410–1414, 2012.

[19] Van Den Broek, S.P. Volume Conduction Effects in EEG and MEG, Ph.D. Thesis, Universiteit Twente, Enschede, The Netherlands, 1997.

[20] Vargas, F. Estimación a posteriori del error y esquemas adaptativos para la solución por elementos finitos de problemas de electroencefalografía. Mathematical Engineering thesis, Universidad de Concepción, Chile, 2014. Available from: `http://www.ing-mat.udec.cl/~rodolfo/Tesis/Memoria_Titulo_Felipe_Vargas.pdf`

[21] Wolters C.H., Influence of Tissue Conductivity Inhomogeneity and Anisotropy on EEG/MEG based Source Localization in the Human Brain. Ph.D. Thesis, University of Leipzig, Germany, 2003.

[22] Wolters C.H., Köstler H., Möller C., Härdtlein J., Grasedyck L. and Hackbusch W. Numerical mathematics of the subtraction method for the modeling of a current dipole in EEG source reconstruction using finite element head models. SIAM J. Sci. Comput. 30(1):24–45, 2007.

Department of Mathematics, University of Trento, Italy
E-mail: alonso@science.unitn.it
URL: http://http://www.science.unitn.it/∼alonso/

Departamento de Matemática y Física Aplicadas, Universidad Católica de la Santísima Concepción, Chile, CI^{2}MA
E-mail: jecamano@ucsc.cl

CI^{2}MA, Departamento de Ingeniería Matemática, Universidad de Concepción, Chile
E-mail: rodolfo@ing-mat.udec.cl
URL: http://http://www.ing-mat.udec.cl/∼rodolfo/

Department of Mathematics, University of Trento, Italy
E-mail: valli@science.unitn.it
URL: http://http://www.science.unitn.it/∼valli/